



In-situ laser ultrasonic grain size measurement in superalloy INCONEL 718



Thomas Garcin ^{a,*}, Jean Hubert Schmitt ^b, Matthias Militzer ^a

^a The Centre for Metallurgical Process Engineering, The University of British Columbia, 309-6350 Stores Rd., Vancouver, BC, V6T 1Z4 Canada

^b MSSMat, CNRS, CentraleSupélec, Université Paris-Saclay, 92290 Châtenay-Malabry, France

ARTICLE INFO

Article history:

Received 8 October 2015

Received in revised form

21 January 2016

Accepted 27 January 2016

Available online 2 February 2016

Keywords:

Laser ultrasonics

Inconel 718

Superalloy

Ultrasound attenuation

Grain growth

ABSTRACT

The nickel-base superalloy, Inconel 718, is widely used in aircraft engines. The control of its final microstructure requires detailed knowledge on recrystallization, grain growth and second phase evolution during thermomechanical processing. The present study focuses on the *in-situ* evaluation of heterogeneous grain growth in the super- δ -solvus domain (above 1050 °C) using laser ultrasonics. This technology is dedicated to the ultrasonic characterization of microstructure evolution during thermo-mechanical processing of metals and alloys. The real time measurement of the ultrasonic attenuation provides the evolution of a representative grain size in the material. A criterion is developed to determine the onset and completion of heterogeneous grain growth stages associated with the dissolution of precipitates. The laser ultrasonic methodology is validated with *ex-situ* metallographic observations and quantitative characterization of the grain size heterogeneity.

© 2016 Elsevier B.V. All rights reserved.

1. Introduction

The development of superalloys has greatly contributed to the improvement of gas turbine jet engines used in the aeronautic industry [1]. Superalloys made with 80% nickel and 20% chromium were developed in the first half of the 20th century and could support combustion temperatures as high as 780 °C when alloyed with small quantities of aluminum and titanium. These alloys were further optimized in the 1950's with the introduction of vacuum induction melting and vacuum arc melting technologies providing a better control in the alloy chemistries and thus improving the mechanical properties. The Inconel 718 alloys were developed in the 1960's as a new class of superalloys containing a large fraction of niobium and tantalum for the precipitation of a second phase with high hardenability. These alloys represent now 60% in weight of the materials used for moving parts of turbo jet engines [1,2]. The Inconel 718 alloys are usually produced by casting, homogenization and hot-forging [3]. The final grain structure is controlled by recrystallization and grain growth occurring during hot-forging operation. One primary source of strengthening in these alloys arises from the precipitation of the nanometric γ' and γ'' phases

which generally form below 850 °C and 925 °C, respectively, upon final cooling. Another important part of the hardening is associated with the presence of the micrometric δ -phase precipitates. These precipitates limit grain growth during hot forging and fine grain sizes contribute to the strengthening of the alloy through the Hall-Petch effect [4]. It was shown that the best resistance to fatigue is obtained for grain sizes ranging from 5 to 40 μm [5]. The grain size distribution is, however, broader when hot forging occurs in the presence of δ -phase precipitates due to their influence on recrystallization and subsequent grain growth [6–8]. Typically, the final grain size for pieces forged in the super- δ -solvus (above the δ -phase dissolution temperature) is in the order of 50–200 μm and ranges from 5 to 50 μm when forging operation occurs in the sub- δ -solvus (below the δ -phase dissolution temperature). Other studies have shown that the control of the initial grain structure prior to forging plays an important role in the completion of recrystallization and obtaining a homogeneous grain structure [9–11]. To further optimize alloying and processing strategies, it is crucial to quantify in detail the grain growth behavior of Inconel 718 alloys. In particular, it is critical to identify heterogeneous grain growth stages that proper heat treatment paths can be designed which lead to homogeneous rather than heterogeneous grain structures.

Conventional methods for investigating microstructure evolution during thermo-mechanical simulations use *ex-situ* examination of the microstructure after quenching. This methodology

* Corresponding author.

E-mail address: thomas.garcin@ubc.ca (T. Garcin).

together with the analysis of flow stress curves can be time consuming as a number of experiments is necessary to quantify microstructure evolution at different stages of the forming process. Moreover, it requires multiple samples for the different interrupted experiments which potentially increases the scattering in the data. Recently, the laser ultrasonic technique was developed for *in-situ* quantification of microstructure evolution in metals and alloys [12]. The technique uses lasers for the generation and detection of ultrasound waves in the material [13]. It is particularly adapted for measurements at high temperature due to the non-contact nature of the sensor. In elastically anisotropic materials, the ultrasound velocity depends, in addition to crystal structure, on the bulk texture in the sample [14] and the ultrasound attenuation is related to the mean grain size [15,16]. Grain growth, phase transformation and recrystallization phenomena can be monitored by this technique. Up to now, it has been mainly used in steel for the investigation of grain size evolution in austenite during static recrystallization [17] and grain growth stages [18] as well as for monitoring austenite decomposition [19]. Further, this technique has also shown great potential for other materials such as commercially pure nickel [20], aluminum alloys [21,22] and zirconium alloys [23].

In the present work, the laser ultrasonic technique is used to monitor the grain size evolution in an Inconel 718 alloy. The measurements are carried out during classical heat treatment schedules including isothermal holding in the super- δ -solvus temperature range. This first step toward a broader use of this technology aims to validate the use of laser ultrasonics for grain size measurements in Inconel 718. Further, these tests simulate the thermal treatment that precedes the forging operation and during which preferential grain growth occurs locally as a result of heterogeneous dissolution of the δ -phase precipitates. The capability of capturing the heterogeneous grain growth stage *in-situ* is validated with *ex-situ* metallographic studies. The present study builds on preliminary work previously published [24].

2. Experimental procedure

The material used for this study is an Inconel 718 superalloy supplied by Aubert & Duval (France). The alloy chemistry in terms of its minimum and maximum weight concentration is indicated in Table 1. The as-received material is composed of polygonal grains with δ -phase precipitates mostly located along grain boundaries. The fraction of the δ -phase was reported to be about 3% for this alloy [25]. Cylindrical samples with a diameter of 10 mm and a length of 15 mm were machined for the experiments.

Experiments were conducted in a Gleeble 3500 thermo-mechanical simulator (Dynamic System Inc. Poestenkill, NY) equipped with a Laser Ultrasonics for Metallurgy (LUMet) sensor. The LUMet sensor is attached to the rear door of the Gleeble chamber. In this sensor, a frequency-doubled Q-switched Nd:YAG laser with a wavelength of 532 nm is used for the generation of a

wide band compressive ultrasound pulse. The duration of the laser pulse is approximately 6 ns, it has a maximum energy of 72 mJ and up to 50 pulses can be generated per second. The laser pulse produces a broadband ultrasound pulse by vaporizing a small quantity of material at the surface (of the order of a micrometer per hundred laser pulses). The ultrasound pulse propagates back and forth through the diameter of the sample and its amplitude decreases by interacting with the material and its microstructure [12–24]. Successive arrivals of the ultrasound pulse at the generation surface are detected with a frequency-stabilized Nd:YAG pulsed laser which illuminates the surface 50 times per second, with an infrared radiation at a wave length of 1064 μm and a pulse duration of 90 μs . The infrared detection laser light reflected on the specimen surface is demodulated inside a photo-refractive crystal using an active interferometer approach [26]. The ultrasound properties measured in this technique are representative of the average properties of the material over a volume created by the surface of the laser spot (about 2 mm) multiplied by the sample diameter. Both generation and detection laser beams are collinearly aligned at the center length of the sample. In the present configuration, the available ultrasonic bandwidth ranges from 2 to 11 MHz and the frequency resolution is 1.5 MHz. The analysis of ultrasound waveform is conducted with the CTOME analysis software [27]. The frequency dependence of the ultrasound attenuation measured *in-situ* during the treatment at high temperature is then correlated with the variation in the mean grain size of the material [16].

Isothermal grain growth was studied *in-situ* and *ex-situ* at 1050 °C, i.e. a temperature where the δ -precipitates dissolve. Prior to the tests, the sample chamber is evacuated down to 0.5 Pa and backfilled with high purity argon gas. The temperature of the sample is measured and controlled with a pair of K-Type thermocouples spot-welded at the mid-length of the samples on the opposite side of the laser beams. The ISO-T compression anvils are used for the tests to guaranty good temperature homogeneity along the long axis of the sample. The temperature difference along the length of the sample is less than 5 °C. A small compression force (~300 N) is maintained to hold the sample in place between the two tungsten carbide anvils. For the grain growth tests, the samples were heated at 10 °C/s to 1000 °C then at a rate of 5 °C/s to 1050 °C in order to avoid a temperature overshoot. The samples were held at 1050 °C for different times and then quenched with helium gas to room temperature. Holding times were set to 0, 30, 75, 130, 175, 230, 480 and 900 s. The cooling rate measured at the surface of the sample was 100 °C/s in the temperature range of 1050 °C–500 °C and decreases as the temperature approaches room temperature.

As validation of laser ultrasonic measurements, the microstructure of each sample was analyzed by conventional *ex-situ* metallography. Samples were cut perpendicularly to the long axis of the cylinder in the plane of the ultrasound wave propagation. The sample preparation for optical metallography consists of conventional grinding, polishing and etching techniques, as reported in detail elsewhere [24]. Further, areas of 1.4 mm by 1.4 mm were characterized using Electron Back-Scattering Diffraction (EBSD). The EBSD system is a DigiView IV EBSD Camera from EDAX attached to a Carl Zeiss NTS Ltd. Sigma field emission scanning electron microscope. Sample surfaces were polished with a finishing solution of colloidal silica. The step size used during EBSD scanning was 1 μm . Analysis is performed with TSL OIM Data Analysis software. Two operations were applied successively to accurately define the position of grain boundaries from the inverse pole figure maps: i) A grain confidence index standardization algorithm uses information on neighbor pixels to apply a correction on pixels indexed with poor confidence generally located near boundaries, ii) The grain dilation algorithm ensures that each grain contains at least 5 pixel located on more than one single row. The

Table 1
Chemical composition (in weight) minimal and maximal of the Inconel 718.

Element	Min	Max
Ni	50	55
Fe	bal	bal
Cr	17	21
Mo	2.8	3.3
Nb + Ta	4.8	5.5
Ti	0.7	1.2
Al	0.4	0.8
Co	0	1

area of each grain was extracted and the mean equivalent area diameter ($EQAD$) is calculated as $(4\bar{A}/\pi)^{0.5}$ where \bar{A} is the arithmetic average of the grain areas. In addition to the $EQAD$, the maximum grain diameter (D_{MAX}) is considered in the analysis as obtained by calculating the average of the 1% largest grain diameters. Further, twins are included in the calculation of mean and maximum grain sizes.

3. Results

3.1. Ex-situ metallography

The optical micrographs of the as-received sample and the one obtained after holding for 175 s at 1050 °C are shown in Fig. 1. In the as-received sample (Fig. 1a), the δ -phase precipitates are present mainly along grain boundaries. After a holding time of 175 s (Fig. 1b), only a very small density of precipitates is visible in the microstructure. Similar dissolution kinetics were previously reported for the δ -phase in these alloys during soaking in the super- δ -solvus temperature range [25,28–31]. The dissolution of the δ -phase leads to a heterogeneous grain growth stage with a wider grain size distribution [24].

In order to evaluate in more detail the occurrence of the heterogeneous grain growth stage, the microstructures of selected samples are analyzed with EBSD mapping. Fig. 2a shows the inverse pole figure map of the initial microstructure. Due to their relatively small size, the δ -phase precipitates are detected with at most two pixels per particles and are removed during the post treatment of the maps. Fig. 2b1, 2c1 and 2d1 show selected inverse pole figure maps of the microstructure quenched-in after various times. After 75 s of holding at 1050 °C, the grains have started to grow only in some regions forming clusters of large grains surrounded by a matrix of small grains. This stage of heterogeneous grain growth is also visible on the samples hold for 175 s. In this sample, clusters of small grains remain surrounded by a matrix of large grains. For times larger than 175 s (e.g. 900 s, see Fig. 2d1), the grain structure

is dominated by the large grains with very few small grains remaining that are randomly dispersed in the structure.

Data collected from the EBSD investigation are reported in Table 2. The $EQAD$ provides a confirmation that the mean grain size increases during the thermal treatment by a factor of about 3. The $EQAD$ values measured by EBSD are systematically smaller than those reported previously from optical metallography [24], reflecting a better capability of the EBSD technique to detect smaller grains. The ratio of $D_{MAX}/EQAD$ indicated in Table 2 provides a representative evaluation of the width of the grain size distribution. The heterogeneity of grain growth is highlighted by the evolution of this ratio during soaking, i.e. $D_{MAX}/EQAD$ increases rapidly during the initial stages of the heat treatment from 3.7 to about 7 before decreasing to about 4, i.e. a similar value than the initial one, and remains constant at longer holding times. These variations are directly related to the formation of clusters of large grains in the structure during the early stages of grain growth.

To quantify the area of the clusters of large grains, a threshold methodology is introduced and applied to the EBSD data. The maximum grain diameter measured in the initial structure, D_{MAX}^0 , is used as a threshold value, i.e. the grains with diameters larger than the threshold are included in the clusters of large grains. In order to account for the presence of small individual twins that are present in the large grains, an additional analysis is conducted from the EBSD map. A total number of 400 individual twins are extracted from the various maps and the twinned areas are analyzed in terms of their aspect ratio indicating that 95% of twinned areas have an aspect ratio lower than 0.3. The threshold method is therefore refined by including the objects with an equivalent diameter larger than the value of $D_{MAX}^0 = 56 \mu\text{m}$ or with an aspect ratio lower than 0.3. The area fraction of large grains is defined by the ratio of the threshold area to the total image area. Fig. 2b2, 2c2 and 2d2 show the large grain areas at different soaking times. As reported in Table 2, the area fraction of large grains f_L raises rapidly in the first 175 s of holding. At longer times, the fraction gradually approaches a limiting value of about 0.8. Although this method is capable of accounting for annealing twins present within large grains while eliminating the small polygonal grains from the statistics, the calculated fraction does not reach 1, i.e. small grains remain in the 2D micrographs after extended soaking times. This observation is consistent with the representation of 3D objects in a 2D cut where large grains can appear small when cut close to their corners. It is therefore useful to normalize the fraction measured with the saturation value of 0.8 to define a normalized area fraction f_L^N as reported in Table 2 indicating that 90% of the volume of the sample consists of large grains in the sample held for 175s.

Further, the position of twin boundaries is determined by assuming a tolerance of 5° from the twin misorientation in the nickel system with a rotation angle of 60° about the [111] direction of the lattice. The twin boundary density ρ_{Twin} (length of twin boundaries per unit area for each map) is calculated by dividing the total length of twin boundaries by the total area of the map. The relative fraction of twin f_{Twin} is then defined by the ratio of twin boundary density to the total grain boundary density. The values for f_{Twin} and for ρ_{Twin} are reported in Table 2. In the fine grained microstructure, i.e. for holding time lower than 75 s, the twin density is relatively stable at $0.5 \mu\text{m}^{-1}$. The values decrease for longer holding in the coarser microstructures where the twin density becomes as low as $0.3 \mu\text{m}^{-1}$. Conversely, the relative fraction of twin boundary is larger in the coarse grained microstructure (0.5) than it is in the finer grain microstructure (0.3).

The presence of a tail in the grain size distribution for samples held for 30 and 75 s is further quantified in Fig. 3 where the cumulative volume fraction is plotted with respect to the grain size D expressed in units of the mean grain size ($EQAD$) for each case. In

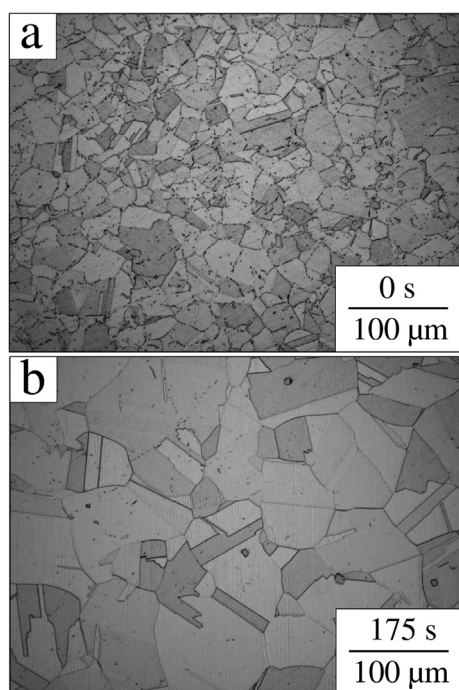


Fig. 1. Optical micrograph of samples hold at 1050 °C and helium quench after a) 0 s and b) 175s.

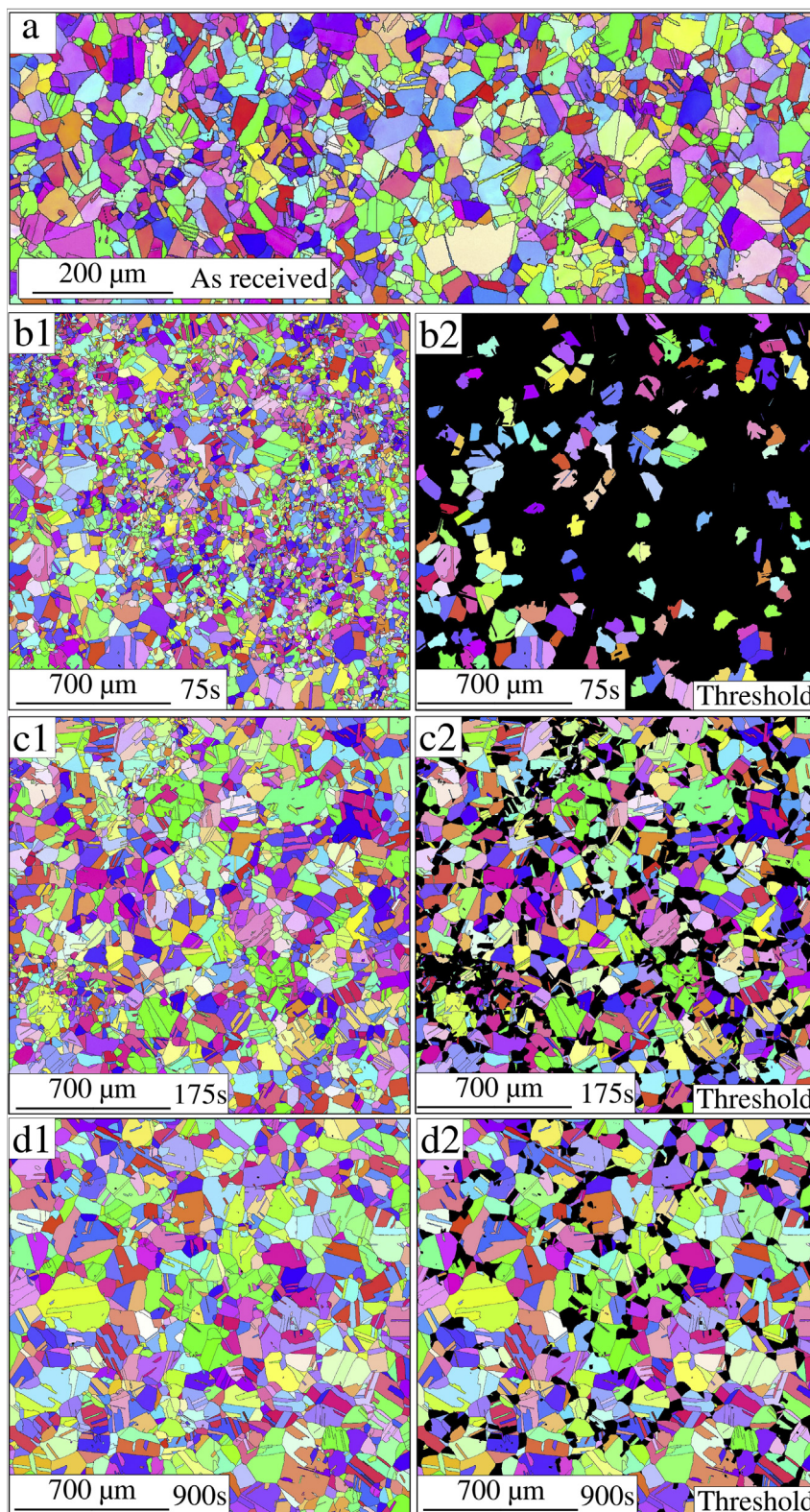


Fig. 2. EBSD maps of a) the initial microstructure and of samples held at 1050 °C and Helium quench after b) 75 s, c) 175 s, and d) 900s. Original images are labeled as b1, c1 and d1; and threshold images for the large grains are labeled as b2, c2, and d2.

this representation, the cumulative volume fraction is quantified from the distribution of third power of the equivalent diameters extracted from the measured grain areas. This representation

allows to test for the self-similarity of the grain size distribution at each time. Clearly, one can observe that the grain size distribution measured in the initial structure and at times larger than 75 s are all

Table 2
Microstructure data obtained from the EBSD investigation.

Time (s)	EQAD(μm)	$D_{\text{MAX}}(\mu\text{m})$	$\frac{D_{\text{MAX}}}{\text{EQAD}}$	f_L	f_L^N	$\rho_{\text{Twin}}(\mu\text{m}^{-1})$	f_{Twin}
0	15	56	3.7	0.02	0.00	0.052	0.30
30	18	120	6.7	0.18	0.20	0.049	0.32
75	19	139	7.3	0.27	0.32	0.053	0.35
175	33	139	4.2	0.73	0.91	0.047	0.53
480	36	155	4.3	0.77	0.96	0.043	0.53
900	42	172	4.1	0.80	1.00	0.031	0.45

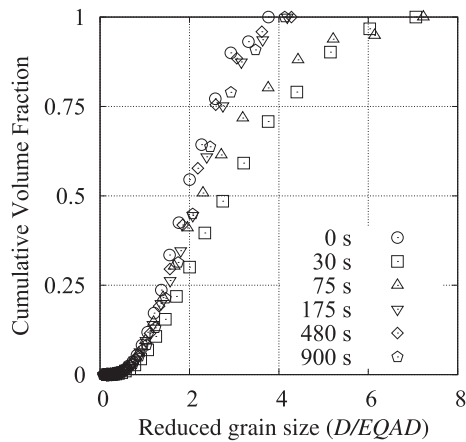


Fig. 3. Cumulative volume fraction with respect to the reduced grain size expressed in units of the mean equivalent area diameter (EQAD).

self-similar. However, the distribution measured at 30 s and 75 s of soaking indicates the presence of large grains occupying a significant volume of the sample.

3.2. Evaluation of the ultrasonic grain size

Fig. 4 shows the ultrasound waveform measured on the cylindrical sample at the beginning of the soaking time, i.e. at $t = 0$ s. Before $3.5 \mu\text{s}$, the signal shows small oscillations corresponding to the residual noise in the system. The first echo of the compressive signal is measured at $4 \mu\text{s}$. After twice this time, the second compressive echo is measured on the ultrasound waveform. Note the inversion of the signal polarity between the first and the second echo typically observed during measurement in a cylinder. The other reflections observed in the signal between the first and second compressive echoes correspond to waves traveling in other directions and/or having other modes of propagation.

Fig. 5a shows the amplitude spectrum of the first echo measured at the end of the holding time for each interrupted treatment. The

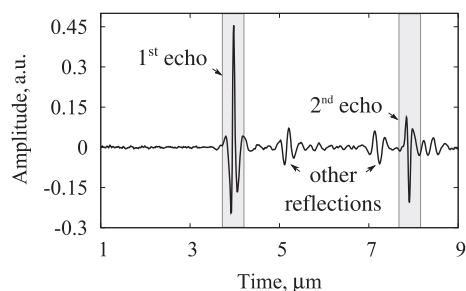


Fig. 4. Ultrasound waveform measured at the beginning of the holding time ($t = 0$ s) at 1050°C .

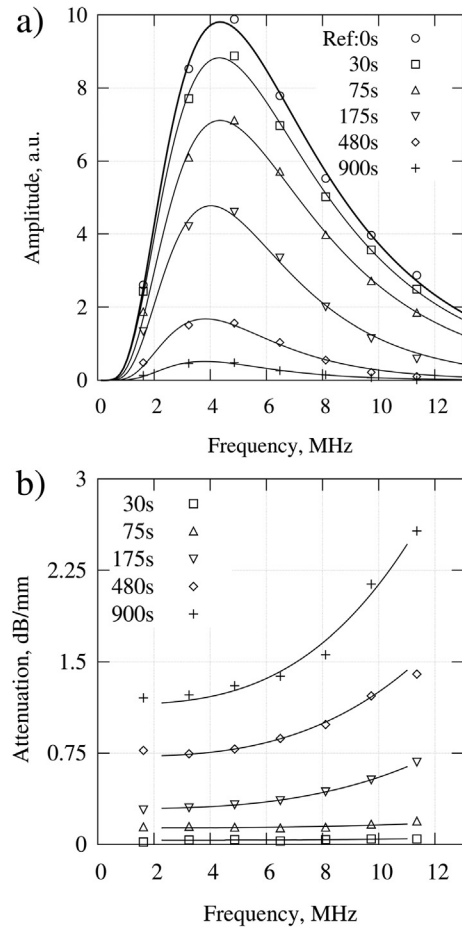


Fig. 5. a) Amplitude spectrum of the first echo of the compressive signal measured after different holding times at 1050°C . b) Ultrasound attenuation spectrum as a function of ultrasound frequency for the different holding times.

amplitude spectrum is plotted with respect to the ultrasound frequency. Its amplitude decreases continuously with time indicating an increase in attenuation. For the compressive wave propagating in the polycrystalline sample, there are generally three main sources of ultrasonic attenuation [17]. The primary contribution is associated with the scattering by grains and is originated by the dispersion of the wave energy due to the elastic mismatch between grains. The second contribution arises from the diffraction of the pulse in the material. The diffraction contribution is generally challenging to quantify accurately as it varies with the geometry of the sample and the propagation distance. The third contribution of attenuation, often of smaller amplitude, is associated with the phenomena causing internal friction in the material.

One method used to quantify the ultrasound attenuation consists of evaluating the amplitude ratio between two successive echoes, i.e. the first and the second echoes of an individual waveform for instance. In this method, the propagation distance for both echoes is different resulting in a significant contribution from diffraction that is then difficult to extract from the grain scattering contribution. A more reliable alternative was therefore introduced to account for this challenge [16,17]. In this second approach, the ultrasound attenuation is calculated by comparing the amplitude spectrum of an echo selected in a waveform measured at time t_i with that measured in a reference sample at a time t_0 such that the attenuation per unit length, expressed in dB/mm, can be defined as:

$$\alpha(f, t_i) = \frac{20}{2m\Theta} \log \left(\frac{A_{Sc}^0(f, t_0)}{A_{Sc}^i(f, t_i)} \right) \quad (1)$$

where f is the ultrasound frequency, Θ is the sample diameter at the measurement temperature, and the amplitude spectrum is A_{Sc}^i for the measured sample with average grain size D_i at time t_i and A_{Sc}^0 for the reference sample with average grain size D_0 at time t_0 . In equation (1), m is the number of the echo selected and here $m = 1$. As both of the ultrasound pulses compared in this method have traveled the same propagation distance, the diffraction contribution is removed from the calculated attenuation. Fig. 5b shows the ultrasound attenuation calculated using the reference at $t = 0$ s. The attenuation spectrum can generally be written as composed of a frequency-dependent “grain size” contribution b and a frequency-independent term a accounting for other contributions which are weakly or non-frequency dependent such as those from internal friction. Under these assumptions, the attenuation can be expressed with a power law of the frequency [15] such as:

$$\alpha(f) = a + bf^n \quad (2)$$

In equation (2), the parameter n is an exponent that varies with the scattering regime, i.e. with the ratio of the ultrasound wavelength to the average grain size in the material [32–34]. In particular, the intensity of grain scattering is associated with the magnitude of the single crystal elastic anisotropy in the material typically quantified by the single crystal anisotropy factor $r = (s_{11} - 2s_{12})/s_{44}$ for cubic crystals, where s_{ij} are the non-zero components of the compliance tensor. The authors found no measurements of the elastic constant of an Inconel 718 single crystal at high temperature. Compliance values are however available up to 1200 °C for a single crystal of Inconel 738 LC [35] from which an anisotropy factor of 3.25 is concluded for 1050 °C. This value is comparable to that of austenite in low alloy steel in the same temperature range [36]. Although the elastic anisotropy may vary slightly with the chemistry of the alloys, this comparison provides reassuring evidence that the scattering by grains in nickel based superalloys has a contribution that is of the same order of magnitude as for austenite in steels for which the technique is well validated. Further, grain sizes in the range of 10–200 μm are also similar to those in austenite of steels and the exponent n in equation (2) is fixed to a value of 3 in order to construct a correlation between the parameter b and the mean grain size in the material [16]. The lines in Fig. 5b show the non-linear regression applied using equation (2) on the experimentally measured attenuation spectrum at various soaking times. The ultrasound attenuation spectrum shows an increasing curvature as the holding time increases, i.e. the frequency dependent parameter b increases with time. The dependence of b for a weakly textured polycrystalline material with polygonal grains has been investigated in detail in the literature [32–34]. The various available models all agree with an expression for the attenuation due to scattering by grains of the form:

$$b(t_i, D_i) = C \left[D_i^{n-1}(t_i) - D_0^{n-1}(t_0) \right] \quad (3)$$

where C is a material and temperature dependent parameter, n is the scattering exponent and the D_i are the EQAD at times t_i . From equations (2) and (3) and using $n = 3$, b can be expressed for convenience as:

$$\sqrt{1000 \cdot b(t_i, D_i)} = C^* \sqrt{D_i^2(t_i) - D_0^2(t_0)} \quad (4)$$

where $C^* = \sqrt{1000C}$. Fig. 6 shows the correlation between the

metallographic grain size (EQAD) indicated in Table 2 and the ultrasound parameter b measured after various holding times at 1050 °C. In order to demonstrate the reliability of the method, the different samples analyzed by EBSD are used as to select the reference grain size in equation (4). The line corresponds to the linear regression applied according to equation (4) and demonstrates that not only the metallographic grain size correlates well with the ultrasonic parameter b but that the correlation is independent of the mean grain size in the reference sample. The value for parameter C^* and its asymptotic standard error are determined to be 0.022 ± 0.001 (5%) when expressing D_i in μm and b in $\text{dB} \cdot \text{mm}^{-1} \cdot \text{MHz}^{-3}$.

This correlation is utilized to evaluate the evolution of the mean grain size during continuous holding at 1050 °C. Fig. 7 shows the entire grain growth curve measured from three LUMet measurements, i.e. for the holding time of 175 s, 480 s and 900 s. The grain sizes measured by metallography are also reported with open circles in the figure. Thanks to the large number of data that can be acquired in real time, the LUMet grain size measurement provides an excellent insight into the grain growth behavior. The different grain growth stages can be clearly observed. Initially, a stage of negligible grain growth occurs for the first 30 s followed by a period of rapid grain growth. Subsequently, i.e. after 230 s, the grain size increases more moderately with time. The rapid grain growth stage coincides with the heterogeneous grain growth stage observed by metallography during which few large grains consume quickly their smaller neighbors.

The vertical error bars indicated in Fig. 6 correspond to the measurement precision for the parameter b and is 15% of the mean value. This precision is estimated by measuring i) the standard deviation of the measured values from sample to sample as well as ii) the standard deviation resulting from measurements of several waveforms in the same sample, i.e. due to various sources of fluctuations inherent to the LUMet technology. The precision in the metallographic grain size obtained by EBSD measurement from the average of more than 2000 grain areas is considered to be small compared to the deviation obtained in the measurement of the ultrasonics parameter. Finally, the resulting precision in the measurement of the relative change in LUMet grain size is linked to the precision of the variable b and C^* . Combining the deviation originated from i) the error in the measurement of b and ii) the goodness of the linear correlation shown in Fig. 6, the precision in the

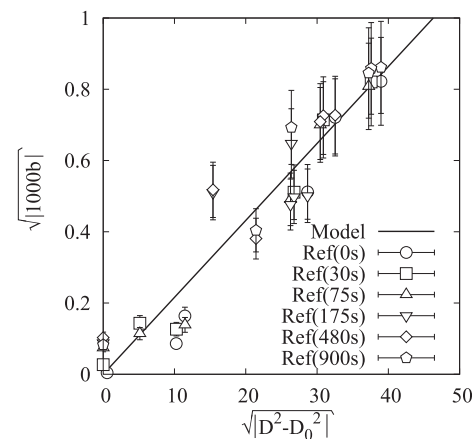


Fig. 6. Correlation between the metallographic grain size (EQAD) and the frequency dependent parameter b measured after various holding times at 1050 °C. The various symbols represent the correlation obtained when different samples are used as reference state in equation (4). The vertical error bar correspond to the precision in the measurement of the parameter b (i.e. 15% of its absolute value).

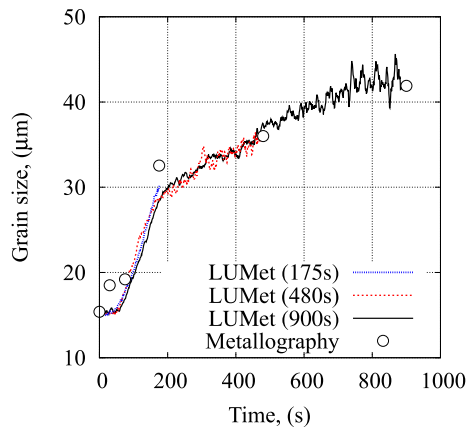


Fig. 7. Mean grain size (EQAD) measured with LUMet (lines) and EBSD metallography during 900 s soaking at 1050 °C.

measurement of the LUMet grain size is estimated by the root mean square of the precision on b and C^* and is 16%.

4. Discussion

The LUMet grain size evolution is measured continuously during the dissolution of the δ -phase precipitates. Once the dissolution is complete, the growth kinetics is controlled only by the grain boundary curvature. During such a grain growth scenario, the mean grain size can be expressed in a first approximation by the general relationship for parabolic grain growth such as:

$$D^2 - D_{init}^2 = Kt \quad (5)$$

where K is an adjustable parameters and D_{init} is the initial grain size for the stage of ideal grain growth. Equation (5) describes well the third stage of grain growth as shown with the black solid line in Fig. 8a. The model parameters in equation (5), i.e. D_{init} and K are summarized in Table 3. In contrast, the first stage of growth needs to be considered with a different approach. The presence of a family of particles pinning the grain boundaries slows down the growth rate and a Zener type pinning model [37] can be applied such as:

$$\frac{dD}{dt} = K \left(\frac{1}{D} - P_0 \right) \quad (6)$$

where P_0 is the pinning pressure. For sake of simplicity, the aim here is to only provide a description of the initial stage of growth during which the population of precipitates remains unchanged resulting in a constant pinning pressure P_0 . In this scenario the grain boundary mobility is assumed to be the same as in the parabolic grain growth model. Integrating the grain growth rate given by equation (6) starting from the initial grain size of 15 μm (see Table 2) the parameter P_0 is adjusted (see Table 3) for the curve to fit the initial evolution of the grain size during the first 30 s (see dashed line in Fig. 8a).

Using these two limiting grain growth scenarios one can now rationalize the rapid grain growth regime at intermediate times. In a first approximation, the fraction of large grains can be obtained by a lever rule method applied using equations (5) and (6) and the LUMet grain sizes measured. Fig. 8b compares the result obtained in this approach (open circles) with the normalized fraction of large grains concluded from metallography (open squares) as reported in Table 2. There is good agreement between the two methods. For holding times larger than 175 s, the attenuation is governed by the

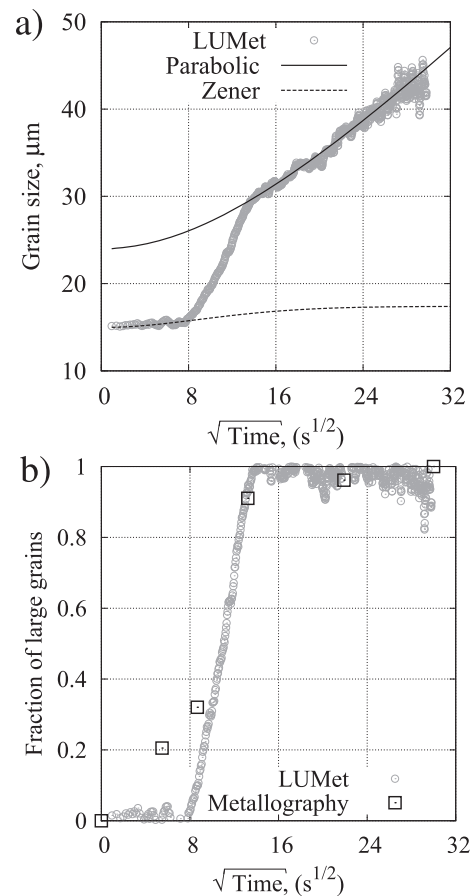


Fig. 8. a) Evolution of the mean grain size (EQAD) during soaking at 1050 °C measured by LUMet (open circles) and parabolic growth model for coarse grains (solid line) as well as Zener pinning model for small grains (dashed line). b) Evolution of the fraction of large grains as obtained from LUMet data (open circles) and metallography (open squares).

Table 3
Numerical values of the fit parameters used in equations (5) and (6).

D_{init} (μm)	K ($\mu\text{m}^2\text{s}^{-1}$)	P_0 (μm^{-1})
24	1.6	0.0574

coarse grains and their growth rate. In this approach, laser ultrasonics allows to quantify the time at which grain growth is no longer affected by the δ -phase particles. In the present case, the evolution of the ultrasonic grain size parameter is a good indicator of the homogeneity of the grain structure within the measured section of the specimen.

5. Conclusions

For the first time, the LUMet system was used for the investigation of grain growth in Inconel 718. The evolution of the grain size was monitored *in-situ* during isothermal holding in the super- δ -solvus region. The following important observations were made:

- 1) The δ -phase precipitates, originally pinning the boundaries, rapidly start to dissolve in the sample at 1050 °C leading to heterogeneous grain growth.

- 2) The ultrasound attenuation can be used to monitor *in situ* the occurrence of this heterogeneous growth stage by a lever rule methodology.
- 3) Ultrasonic measurements can thus be used to quantify the onset and completion of heterogeneous grain growth. This information is of practical importance as it can rapidly give important indication on the grain size evolution during annealing prior to forging where the goal is to obtain a homogeneous grain structure.

Acknowledgments

The authors acknowledge fruitful discussions with Prof. C.W. Sinclair during the course of the study. The financial contributions from the Canadian Foundation of Innovation (CFI) (Project number 21710) and the Natural Science and Engineering Research Council (NSERC) (strategic grant, File number: STPGP 430128 - 12) of Canada are acknowledged with gratitude. The authors thank Aubert&Duval (France) for providing test samples.

References

- [1] R.C. Reed, *The Superalloys: Fundamentals and Applications*, Cambridge University Press, 2006.
- [2] B. Geddes, H. Leon, X. Huang, *Superalloys: Alloying and Performance*, ASM International, 2010.
- [3] R. Cozar, A. Pineau, *Metall. Trans.* 4 (1973) 47–59.
- [4] J. de Jaeger, D. Solas, T. Baudin, O. Fandeur, J.H. Schmitt, C. Rey, *Adv. Mater. Res.* 409 (2011) 751–756.
- [5] N. Spath, V. Zerrouki, P. Poubanne, J.Y. Guedou, *Superalloys*, in: E.A. Loria (Ed.), 706 Var. Deriv, 718, TMS, Warrendale, PA, 2001, pp. 173–183, 625.
- [6] M.S. Lewandowski, R.A. Overfelt, *Acta Mater* 47 (1999) 4695–4710.
- [7] R.A.P. Djaic, J.J. Jonas, *Metall. Trans.* 4 (1973) 621–624.
- [8] N.K. Park, I.S. Kim, Y.S. Na, J.T. Yeom, *J. Mater. Process. Technol.* 111 (2001) 98–102.
- [9] D. Zhao, P.K. Chaudhury, *Superalloys*, in: E.A. Loria (Ed.), 706 Var. Deriv 718, TMS, Warrendale, PA, 1994, pp. 301–313, 625.
- [10] H. Yuan, W.C. Liu, *Mater. Sci. Eng. A* 408 (2005) 281–289.
- [11] S.C. Medeiros, Y.V.R.K. Prasad, W.G. Frazier, R. Srinivasan, *Mater. Sci. Eng. A* 293 (2000) 198–207.
- [12] S.J. Davies, C. Edwards, G.S. Taylor, S.B. Palmer, *J. Phys. D.* 26 (1993) 329–348.
- [13] J.P. Monchalain, *Rev. Quant. Nondestruct. Eval.* 23 (2004) 3–31.
- [14] A. Moreau, D. Lévesque, M. Lord, M. Dubois, J.P. Monchalain, C. Padioleau, J.F. Bussière, *Ultrasonics* 40 (2002) 1047–1056.
- [15] M. Dubois, M. Militzer, A. Moreau, J.F. Bussière, *Scr. Mater* 42 (2000) 867–874.
- [16] S. Kruger, G. Lamouche, J.P. Monchalain, R. Kolark, G. Jeskey, M. Choquet, *Iron Steel Technol.* 2 (2005) 25–31.
- [17] S. Sarkar, A. Moreau, M. Militzer, W.J. Poole, *Metall. Mater. Trans. A* 39 (2008) 897–907.
- [18] M. Maalekian, R. Radis, M. Militzer, A. Moreau, W.J. Poole, *Acta Mater* 60 (2012) 1015–1026.
- [19] S.E. Kruger, E.B. Damm, *Mater. Sci. Eng. A* 425 (2006) 238–243.
- [20] S.E. Kruger, S. Bolognini, G. Lamouche, A. Moreau, in: *Quant. Nondestruct. Eval. AIP Conf. Proceedings*, vol. 615, 2002, pp. 1518–1525.
- [21] S.E. Kruger, A. Moreau, M. Militzer, T. Biggs, *Mater. Sci. Forum* 426 (2003) 483–488.
- [22] A. Moreau, S. Bescond, S. Bolognini, M. Lord, S.E. Kruger, C.S. Man, *ASM International*, in: *Materials Science & Technology Conf. Proceedings*, 2005, pp. 3–10.
- [23] A. Moreau, P.J. Kielczynski, J.F. Bussière, J.H. Root, in: R.E. Green (Ed.), *Non-destruct. Charact. Mater. VI*, Plenum Press, New York, 1994, pp. 119–128.
- [24] T. Garcin, J.H. Schmitt, M. Militzer, in: J.Y. Guédou, J. Choné (Eds.), *MATEC Web of Conferences*, 14, 2014, 07001.
- [25] J. De Jaeger, *Contribution à l'étude métallographique de la recristallisation dynamique de l'Inconel 718 lors du forgeage à chaud: Approches expérimentale et numérique*, Ph.D. Dissertation, Ecole Centrale Paris, 2013.
- [26] R.K. Ing, J.P. Monchalain, *Appl. Phys. Lett.* 59 (1991) 3233–3235.
- [27] T. Garcin, *CTOME V1.52: Software for the Analysis of Ultrasound Wave Properties in Metal*. www.ctome.org.
- [28] S. Azadian, L.Y. Wei, R. Warren, *Mater. Charact.* 53 (2004) 7–16.
- [29] D. Cai, W. Zhang, P. Nie, W. Liu, M. Yao, *Mater. Charact.* 58 (2007) 220–225.
- [30] A.W. Dix, J.M. Hyzak, R.P. Singh, in: E.A. Loria (Ed.), *Superalloys*, TMS, Warrendale, PA, 1992, pp. 23–32.
- [31] V.A. Wills, D.G. McCartney, *Mater. Sci. Eng. A* 145 (1991) 223–232.
- [32] E.P. Papadakis, *J. Acoust. Soc. Am.* 37 (1965) 703–710.
- [33] F.E. Stanke, G.S. Kino, *J. Acoust. Soc. Am.* 75 (1984) 665–681.
- [34] D. Nicoletti, A. Anderson, *J. Acoust. Soc. Am.* 101 (1997) 686–689.
- [35] W. Hermann, H.G. Sockel, J. Han, A. Bertram, in: E.A. Loria (Ed.), *Superalloys*, TMS, Warrendale, PA, 1996, pp. 229–238.
- [36] J. Zarestky, C. Stassis, *Phys. Rev. B* 35 (1987) 4500–4505.
- [37] C. Zener, *Trans. AIME* 175 (1948) 15–51.